CCFE
CULHAM CENTRE FOR FUSION ENERGY

UK Atomic Energy Authority

UKAEA-CCFE-PR(23)112

Megha Sanjeeva, Mark R. Gilbert, Samuel T. Murphy

Thermal conductivity of non-stoichiometric Li2TiO3

Thermal conductivity of non-stoichiometric Li2TiO3

Megha Sanjeeva, Mark R. Gilbert, Samuel T. Murphy

This is a preprint of a paper submitted for publication in
Journal of Nuclear Materials

Thermal conductivity of non-stoichiometric Li_2TiO_3

Megha Sanjeev[a], Mark R. Gilbert[b], Samuel T. Murphy[a,*]

[a] *Engineering Department, Lancaster University, Bailrigg, Lancashire, LA1 4YW, UK*
[b] *CCFE, United Kingdom Atomic Energy Authority, Culham Science Centre, Abingdon, Oxon, OX14 3DB, UK*

Abstract

The transfer of heat through the breeder region of a future fusion reactor is a key component of its thermal efficiency. Development of advanced ceramic breeder materials based on Li_2TiO_3 seek to exploit its ability to accommodate significant non-stochiometry, however, it is not clear how deviations for the 50:50 mix of Li_2O and TiO_2 will affect key properties of the material, including the thermal conductivity. Therefore, in this work molecular dynamics simulations are employed to examine how the thermal conductivity of Li_2TiO_3 changes with stoichiometry. The results suggest that while there is a significant decrease in the thermal conductivity at room temperature, at higher temperatures the impact of deviations from stoichiometry is limited.

1. Introduction

Future fusion power stations will employ the reaction between deuterium and tritium, the so-called D-T reaction. While deuterium can be extracted from sea water, tritium does not occur naturally in sufficient quantities to support a fleet of fusion reactors. Therefore, it will be necessary to breed tritium *in-situ* from the transmutation of lithium, driven by the neutron ejected by the D-T reaction. To achieve this, the fusion plasma chamber will be surrounded by a breeder blanket, which is also used to convert the neutron's energy into heat for electricity generation, as well as helping to shield the magnets and other

*Corresponding author
Email address: samuel.murphy@lancaster.ac.uk (Samuel T. Murphy)

components. To ensure the whole fusion process is sustainable it is essential to be able to recover at least one tritium from the blanket for each fusion reaction occurring in the plasma (in practice, it will be necessary for the tritium breeding ratio or TBR to be somewhat above one to allow for engineering losses in the fuel cycle). The design of the blanket and the selection of materials from which it is to be constructed is therefore a critically important part of a future fusion power station.

There have been a number of different concepts developed for the breeder blanket and these fall into two broad categories defined by the phase of the breeder material itself. Concepts based on solid breeder materials employ ceramic lithium oxides, typically in the form of small pebbles, while liquid concepts utilise a molten lithium-lead eutectic. The lithium ceramics offer high lithium densities and good chemical compatibility with structural materials but their low thermal conductivities result in relatively low thermal efficiencies [1]. By contrast, the liquid concepts offer higher thermal efficiencies but the reactivity of the liquid metal is a concern in the event of an accident.

A number of lithium ceramics have been considered for application in the breeder blanket, including Li_2O, $LiCoO_2$ and Li_2ZrO_3. In recent years attention has focused on lithium metatitanate (Li_2TiO_3) and lithium orthosilicate (Li_4SiO_4) and these have been selected for use in the Test Blanket Modules on ITER. Selection of the leading candidate material and development of the actual breeder blanket requires the ability to predict how the materials evolve during operation, where they will be exposed to high heat fluxes (with temperatures expected to be in the range 300-950°C [2]) and irradiation by high energy neutrons. Most importantly, it is necessary to be able to estimate how key physical properties of the materials will change during operation.

The overall thermal efficiency of the reactor depends on the rate of heat transfer to the coolant, which is determined by a number of factors including the thermal conductivity of the breeder material itself. In general, ceramic oxides have low thermal conductivites due to being insulators and so heat transfer is predominantly facilitated by phonons. Defects introduced into the ceramic

breeder matrix during operation, either from lithium depletion or radiation damage, will act as phonon scattering centres, degrading the thermal conductivity still further. Snead *et al.* explored the relationship between defect density introduced by neutron irradiation and degradation of the thermal conductivity [3]. They observed a sublinear dose dependence in the range 0.001 and 0.01 dpa at low temperature. MD simulations of SiC suggested that the increase in thermal resistivity was proportional to the defect concentrations, however, the factor of this proportionality depended on the specific defect type [4]. At higher temperatures Snead *et al.* demonstrate that the thermal conductivity is closer to the bulk value due to the defect recovery [3]. However, MD simulations of Gd doped UO_2, also showed that impact on the thermal conductivity decreases as a function of temperature [5]. In these simulations the defect population remains roughly constant and so it is clear that recombination is not the sole reason for the recovery in thermal conductivity.

In addition to reducing the heat flow to the coolant the reduction in the thermal conductivity may result in increased thermal stresses in the pebbles that may result in loss of their structural integrity. Therefore, it is essential to be able to determine the thermal conductivity of the material as it is ages. Here we will focus on the titanate.

While there is a metastable cubic phase at low temperatures it is the β-phase that dominates up to temperatures of 1215°C [6]. It is this β-phase that is of interest for tritium breeding. The crystal structure of β-phase Li_2TiO_3 was first determined by Lang [7] and subsequently refined using X-ray diffraction of large single crystals by Kataoka *et al.* [8]. β-Li_2TiO_3 is monoclinic an exhibits the C2/c space group and can be thought of as a disordered rocksalt structure with alternating (111) cation planes of lithium, oxygen and a mixed layer containing both cations. This layered structure results in many of the materials properties being highly anisotropic, see for example the dielectric tensor [9]. An illustration of the unitcell of Li_2TiO_3 is presented in figure 1. Within the unitcell the Li1 and Li2 ions sit in the pure lithium layer and the Li3 ions sit at the centre of the hexagons in the mixed cation layer.

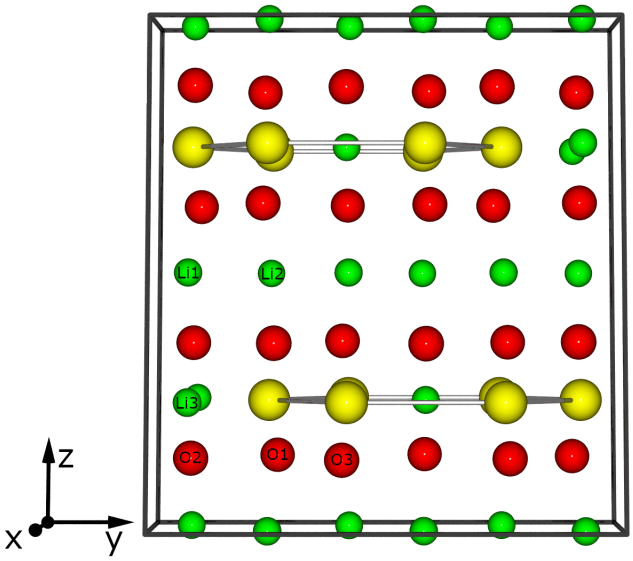

Figure 1: Graphical representation of the unitcell of Li_2TiO_3. Green, yellow and red spheres represent lithium, titanium and oxygen ion respectively.

According to the phase diagram of the Li_2O/TiO_2 system [10, 6], we see that β-Li_2TiO_3 has a compositional homogeneity range of 47 to 51.5 mol% TiO_2. This compositional flexibility has been exploited in the development of advanced ceramic breeder materials such as $Li_{2+x}TiO_{3+y}$ [11, 12, 13, 14], where the increase in lithium density results in improved tritium breeding performance. During operation, lithium will undergo transmutation to generate tritium for the plasma and so the material will be increasingly Li deficient as it ages; Li burn-up may reach several 10s of % during a typical blanket lifetime [15]. Therefore, it is important to be able predict the thermal conductivity of the titanate across a wide stoichiometric range.

The exact mechanisms by which any non-stoichiometry will be accommodated has been examined widely in the literature. A number of different mechanisms have been proposed for accommodation of a lithium excess. Hao *et al.*

[16] and Bian and Dong [17] propose that a lithium excess is accommodated by titanium vacancy V_{Ti}^{4-} defects charge compensated by oxygen vacancies. These defects can be represented using Kroger-Vink notation as V_{Ti}^{4-} and V_{O}^{2+}, where the V indicates a vacancy defect on a site indicated by the subscript. The defect's relative charge is indicated in the superscript [18]. At smaller deviations from stoichiometry Hao *et al.* propose that the Li_i^{1+} defect is the dominant defect for incorporating the lithium excess. This suggestion is supported by the diffraction data of Mukai *et al.* who also suggest the presence of the $\mathrm{Li}_{\mathrm{Ti}}^{3-}$ antisite defect (i.e. where Li sits in a Ti site), which is charge compensated for by reduction of Ti [19]. The presence of lithium substitution onto titanium sites is also supported by the density functional theory (DFT) simulations of Murphy and Hine [20]. There is less disagreement regarding the identification of the dominant defects on the lithium deficient side of the phase diagram, with Yu *et al.* and Murphy and Hine proposing the $\mathrm{Ti}_{\mathrm{Li}}^{3+}$ defect charge compensated for by V_{Li}^{1-} defects. Vitins *et al.* also suggest that the some of the lithium sites become substituted by titanium [21].

Previous studies of the thermal conductivity of Li_2TiO_3 have shown significant variation arising due to different pebble sizes, densities and compositions [22, 23, 24]. Interestingly, the thermal conductivities determined by Hoshino [11] and Roux [25] for lithium deficient Li_2TiO_3 are greater than values previously determined for the stochiometric material. Similarly, Mukai *et al.* observe an increased thermal diffusivity for lithium rich samples [19]. As stated above, the introduction of an increased concentration of point defects to accommodate this non-stoichiometry would be expected to reduce the thermal conductivity and diffusivity. Mukai *et al.* argue that the origin of the increase is due to the microstructure, as the Li-rich samples are much closer to the theoretical density, and not the thermal conductivity through the grains themselves [19]. Therefore, this still leaves the question of how significant the change in the thermal conductivity in the fuel grains themselves is.

As discussed above the previous experiments attribute the increase in the thermal conductivity/diffusivity to changes in the microstructure that arises

for the different stoichiometries. This makes it difficult to determine how the thermal conductivity will change in a pebble that starts with the microstructure corresponding to an Li-rich or stoichiometric composition and then moves to become lithium deficient. This type of information can be determined with an atomic resolution using atomistic simulation techniques, like molecular dynamics. Classical MD has already been employed to demonstrate the highly anisotropic thermal conductivity in Li_2TiO_3 [26]. Therefore the aim of this work is to use MD to understand how the introduction of non-stoichiometry changes the thermal conductivity of bulk Li_2TiO_3.

2. Methodology

Determination of how changes in stoichiometry will affect the thermal conductivity of Li_2TiO_3 will be achieved in two steps. In the first step we will use lattice statics techniques to understand how the changes in stoichiometry are incorporated in the lattice. For the calculation of the impact of this non-stoichiometry on the thermal conductivity we will perform molecular dynamics simulations using supercells seeded with the defects predicted from step 1.

2.1. Modelling interatomic interactions

All simulations presented here envisage the crystal as an infinite array of point charges as proposed by Born [27]. The interactions between atoms were represented using a combination of a long range Coulombic potential and a short range empirical potential, of the Buckingham form [28], as parameterised by Vijayakumar *et al* [29]. This potential is a development of the highly successful Matsui potential for TiO_2 [30]. As generated, the model assigns partial charges to the ions such that $q_{\mathrm{Li}} = 0.549\|e\|$, $q_{\mathrm{Ti}} = 2.196\|e\|$ and $q_{\mathrm{O}} = -1.098\|e\|$. The shell model of Dick and Overhauser [31] was used to represent the polarisability of the oxygen ions. The efficacy of the potential to represent the different phases of Li_2TiO_3 is discussed in detail in previous work [32]. The use of shells in molecular dynamics simulations requires shell masses to arbitrarily be assigned

or for the energy minimisation of core-shell separations at each timestep, which is computationally expensive. In this work the empirical model is employed without shells. In order to demonstrate the efficacy of the potential model used here the lattice parameters are compared to experimental values in table 1:

Table 1: Table of lattice parameters and elastic constants as obtained from the empirical model with shells off (this work), empirical model with shells on [32], density functional theory [32] and experiment [8].

Property	Emp (shells off)	Emp (shells on)	DFT	Exp
a /Å	5.10	5.07	5.09	5.06
b /Å	8.85	8.80	8.83	8.79
c /Å	9.48	9.51	9.51	9.75
α /°	90.00	90.00	90.00	90.00
β /°	100.32	100.24	100.25	100.21
γ /°	90.00	90.00	90.00	90.00

2.2. Lattice statics simulations

Calculation of the defect energies were performed using the Mott-Littleton approach [33] and the GULP simulation package [34]. In the Mott-Littleton method the lattice is partitioned into three concentric regions (1, 2a and 2b) centered on the defect of interest. Within the central region, with a radius of 10 Å, ions are treated using the potential and are relaxed to achieve a force balance. The ions of region 2a are relaxed in one step using the Mott-Littleton approximation with the interactions between the regions treated explicitly. This region extended for 20 Å beyond region 1. The remainder of the crystal (region 2b) is simply represented as an array of point charges and is used to generate the Madelung field of the crystal.

2.3. Thermal conductivity simulations

Molecular dynamics simulations were performed using the LAMMPS simulation package [35]. Simulation supercells were constructed by taking L repeti-

tions of the Li_2TiO_3 supercell along the direction of interest, and 10×10 unitcell cross-sections. These simulation supercells are initially energy minimised under constant pressure and subsequently equilibrated for 50,000 timesteps of 2 fs each, under constant pressure and temperature (NPT) conditions using a Nose-Hoover style thermostat and barostat with relaxation times of 0.05 ps and 1.0 ps, respectively.

Once equilibrated, the thermal conductivity was determined using the Müller-Plathe method [36], which is a Non-Equilbrium Molecular Dynamics (NEMD) approach. The method divides the supercell into "chunks" along the direction of calculation. Kinetic energy swaps are then performed between the hottest atom in the "cold chunk" and the coldest atom in the "hot chunk" by swapping the velocity of the atoms. The energy cost of each swap (Q) is logged, and the process is repeated until a steady state temperature gradient (∇T) is created. The thermal conductivity (k) is then simply calculated using Fourier's law ($Q = k\nabla T$) [37].

In this work, the supercell was divided into 20 "chunks" along L, the chosen direction of calculation. The kinetic energy swaps were performed every 10 timesteps under constant volume and energy (NVE) conditions, along L. After allowing for at least 100,000 timesteps for the temperature gradient to form, the temperature of each chunk is recorded every 1000 timesteps for a further 100,000 timesteps. The average temperature gradient over these last 100,000 timesteps is then fitted to a straight line using the method of least squares from which the thermal conductivity is finally calculated. This is the same procedure as followed in previous work calculating thermal conductivity of perfect Li_2TiO_3 [26].

In crystalline structures, the calculated thermal conductivity shows a dependence on the size of the simulation supercell. This is the result of phonon scattering due to the supercell length L restricting the mean free path of the phonons [38, 39]. To avoid this without succumbing to the high computational costs of increasing cell sizes, we employ an extrapolation procedure [40, 39],

using the following relationship,

$$\frac{1}{k} \propto \frac{1}{L} \tag{1}$$

between the thermal conductivity and supercell length.

By calculating the thermal conductivity for a range of increasing supercell lengths (L = 30, 40, 50, and 100 unitcell lengths) a final value of the thermal conductivity is obtained by extrapolating the calculated value.

3. Results & Discussion

3.1. Defects and non-stoichiometry

To determine the exact mechanisms responsible for accommodating non-stoichiometry it is essential to know the energies for all of the intrinsic defect species. For Li_2TiO_3 these are presented in table 2. Defect energies calculated using the Mott-Littleton approach represent the energy to add or remove atoms and any accompanying charge from the system and placing them at an infinite separation, where they no longer interact with the system or each other. Consequently, they are not directly comparable with formation energies calculated using DFT where a reference state for both the atoms and electrons is typically defined. However, it is possible to draw comparisons between defects of the same type. For example, table 2 shows that the lithium site in the mixed cation layer (V^{1-}_{Li3}) exhibits the lowest defect energy of the lithium vacancy defects in excellent agreement with previous DFT simulations. There are small discrepancies with the DFT in that table 2 predicts that the $\mathrm{V}^{1+}_{\mathrm{Li2}}$ defect is lower in energy than the $\mathrm{V}^{1+}_{\mathrm{Li1}}$ defect, while the DFT predicts the opposite ordering [20]. It is noted here that the difference in energy for these two vacancy defects presented here is 0.03 eV and for the DFT it is 0.04 eV, which is within the expected error of both techniques implying that the energy for the two defects are essentially the same.

Substitution of a titanium ion onto the lithium site in the mixed cation layer has a slightly larger defect energy than for substitution into the pure Li layer.

Table 2: Table showing the defect energies for the intrinsic defects in Li_2TiO_3– as calculated using molecular simulations with the empirical potentials described in the text.

Defect	Defect energy /eV	Defect	Defect energy /eV
V_{Li1}^{1-}	3.21	$\mathrm{Li}_{\mathrm{Ti1}}^{3-}$	27.59
V_{Li2}^{1-}	3.18	$\mathrm{Li}_{\mathrm{Ti2}}^{3-}$	27.59
V_{Li3}^{1-}	3.01	Li_{i1}^{1+}	-2.02
V_{Ti1}^{4-}	32.13	Li_{i2}^{1+}	-2.00
V_{Ti2}^{4-}	32.13	Ti_{i1}^{4+}	-22.23
V_{O1}^{2+}	9.22	Ti_{i2}^{4+}	-24.14
V_{O2}^{2+}	9.16	O_{i1}^{2-}	-0.99
V_{O3}^{2+}	9.43	O_{i2}^{2-}	-0.99
$\mathrm{Ti}_{\mathrm{Li1}}^{3+}$	-23.00		
$\mathrm{Ti}_{\mathrm{Li2}}^{3+}$	-22.90		
$\mathrm{Ti}_{\mathrm{Li3}}^{3+}$	-22.42		

This is likely due to the greater repulsion from the Ti^{4+} ions in the mixed cation layer and again concurs with existing DFT data [32]. For the oxygen vacancy defects, previous DFT simulations have shown that the removal of the oxygen from the O3 site is less energetically favourable than removal from either the O1 or O2 sites. Table 2 shows that the defect energy for the V_{O3}^{2+} defect is 9.43 eV which is higher than the values of 9.22 eV and 9.16 eV predicted for the V_{O1}^{2+} and V_{O2}^{2+} defect respectively, therefore it agrees with DFT. The empirical potential also predicts that there is very little distinction between the titanium sites, as the defect energies for the vacancy and antisite defects are the same on both available sites.

The crystal structure of Li_2TiO_3 means that the interstitial defects display complex geometries. For lithium the lowest energy interstitial defect has a split structure similar to those predicted in other materials [41]. Figure 2 shows the lowest energy Li interstitial defect aligned along the z-direction centered on the

Li3 site in the mixed cation layer. This interstitial configuration is only 0.02 eV lower than the simple isolated interstitial. A number of other split interstitial configurations were observed, aligned along different crystallographic directions, however, only the two lowest energies are reported in table 2 for conciseness. The titanium interstitial is predicted to be metastable and will displace a lithium ion resulting in the formation of a titanium antisite and lithium interstitial, i.e.:

$$\mathrm{Ti}_i^{4+} + \mathrm{Li}_{\mathrm{Li}}^{\times} \rightarrow \mathrm{Ti}_{\mathrm{Li}}^{3+} + \mathrm{Li}_i^{1+}. \tag{2}$$

The energy for this reaction is predicted to be -2.16 eV.

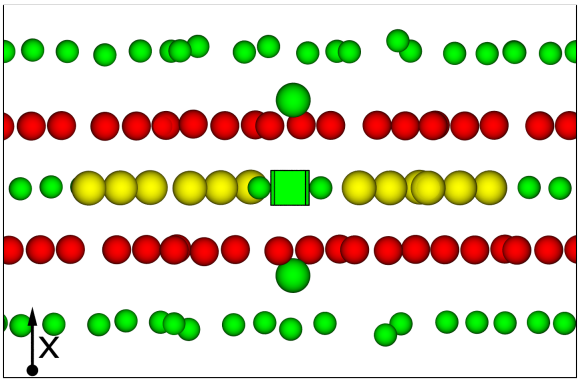

Figure 2: Graphical representation of the lowest energy Li_i^{1+} defect. Green, yellow and red spheres represent the lithium, titanium and oxygen ions respectively. The lithium interstitial displaces another lithium ion from the Li3 lattice site to create a Li^{1+}:V_{Li}^{1-}:Li^{1+} defect cluster aligned along the [001] direction, where the lithium vacancy is represented by the transparent green cube.

With the defect formation energies presented in table 2 it is possible to calculate the reaction energies for the intrinsic defect processes. The per defect reaction energies for the intrinsic defect processes are presented in table 3. The results show that the lithium Frenkel process is the lowest energy process and the antisite process is the next lowest energy process. Therefore, the defect chemistry would be expected to be dominated by lithium interstitials/vacancies and antisite defects as predicted by DFT [32].

Table 3: Table showing the reaction energies of rate intrinsic defect processes in Li_2TiO_3 normalised per defect (i.e. reaction energy/number of defects).

Process	Reaction energy /eV
Li Frenkel	0.49
O Frenkel	4.03
Ti Frenkel	4.62
Antisite	2.29
Schottky	10.93

There are a range of different processes responsible for the accommodation of excess Li_2O and TiO_2 in Li_2TiO_3. In the majority of cases there is the defect that actually accommodates the excess cation and then other defects that compensate for the charge imbalance that arises, for example excess lithium might be accommodated via the Li_{Ti}^{3-} defect with charge compensation provided by the V_O^{2+} defect. Therefore, by considering all accommodating defects compensated for by all possible oppositely charged defects (while still ensuring the overall reaction changes the stoichiometry) it is possible to write a series of reactions that can accommodate non-stoichiometry in Li_2TiO_3. The list of processes considered in this work and the energy per formula unit incorporated into Li_2TiO_3 are presented in table 4. Note that in all cases the lowest energy for each defect has been used in the calculation of the reaction energies.

The results presented in table 4 show that the most thermodynamically favourable process for introducing excess Li_2O into Li_2TiO_3 is via a combination of the Li_i^{1+} and Li_{Ti}^{3+} defects. This prediction is in excellent agreement with previous DFT studies that predict that excess Li_2O incorporation by the same defects at intermediate oxygen partial pressures [20]. On the other side of the Li_2O-TiO_2 phase diagram the lowest energy process for incorporation of excess TiO_2 is via reaction 10 in the table. In reaction 10 excess TiO_2 is accommodated by the mutually charge compensating V_{Li}^{1-} and Ti_{Li}^{3+} defects,

Table 4: Reaction energies for the incorporation of non-stoichiometry into Li_2TiO_3.

Excess	Number	Reaction	Reaction energy per Li_2O/TiO_2 /eV
Li_2O	1	$Li_2O_{(s)} \rightarrow 2Li_i^{1+} + O_i^{2-}$	5.13
	2	$3Li_2O_{(s)} + Ti_{Ti}^0 \rightarrow 4Li_i^{1+} + V_{Ti}^{4-} + Li_2TiO_{3(s)}$	1.55
	3	$3Li_2O_{(s)} + Ti_{Ti}^0 \rightarrow 3Li_i^{1+} + Li_{Ti}^{3-} + Li_2TiO_{3(s)}$	0.72
	4	$6Li_2O_{(s)} + 4Ti_{Ti}^0 + 6O_O^0 \rightarrow 4Li_{Ti}^{3-} + 6V_O^{2+} + 4Li_2TiO_{3(s)}$	4.42
	5	$3Li_2O_{(s)} + 4Ti_{Ti}^0 \rightarrow 4Li_{Ti}^{3-} + 3Ti_i^{4+} + Li_2TiO_{3(s)}$	8.87
	6	$Li_2O_{(s)} + Ti_{Ti}^0 + 2O_O^0 \rightarrow V_{Ti}^{4-} + V_O^{2+} + Li_2TiO_{3(s)}$	10.63
TiO_2	7	$TiO_{2(s)} \rightarrow Ti_i^{4+} + 2O_i^{2-}$	16.14
	8	$3TiO_{2(s)} + 4Li_{Li}^0 \rightarrow Ti_i^{4+} + 4V_{Li}^{1-} + 2Li_2TiO_{3(s)}$	3.45
	9	$3TiO_{2(s)} + 2Li_{Li}^0 \rightarrow 2Ti_{Li}^{3+} + 3O_i^{2-} + Li_2TiO_{3(s)}$	6.63
	10	$6TiO_{2(s)} + 8Li_{Li}^0 \rightarrow 2Ti_{Li}^{3+} + 6V_{Li}^{1-} + 4Li_2TiO_{3(s)}$	1.67
	11	$TiO_{2(s)} + 2Li_{Li}^0 + O_O^0 \rightarrow 2V_{Li}^{1-} + V_O^{2+} + Li_2TiO_{3(s)}$	4.76

in agreement with previous studies [20, 42]. Overall, table 4 shows that the energy required to incorporate one formula unit of Li_2O is nearly 0.8 eV lower than for the incorporation of a TiO_2 unit. This observation matches the phase diagram presented in reference 6 that shows that Li_2TiO_3 can accommodate a greater degree of excess Li_2O than TiO_2. Overall the potential appears to very accurately reproduce the defect chemistry of Li_2TiO_3 from both experiment and DFT.

3.2. Thermal conductivity of non-stoichiometric Li_2TiO_3

Using the predictions above we can create simulation supercells for molecular dynamics that contain representative degrees of non-stoichiometry. To explore both sides of the stoichiometry regime we look at 1% Li_2O excess (Li-rich) and 1% TiO_2 excess (Li-poor) and use reaction numbers 3 and 10, respectively (see table 4).

For the Li-rich case, 0.5% of Ti sites were randomly selected and substituted with Li. Then, three times as many Li interstitials were added to make up to 1% Li excess while ensuring charge neutrality. For the Li-poor case, 0.25% of Li sites were randomly selected and substituted with Ti. Then, three times as many Li vacancies were created to balance the charge and make up to 1% lithium loss. The defects were randomly introduced into the simulation supercells using Atomsk [43]. As the non-stoichiometry is accommodated by charged defects it is likely that these defects will form clusters, particularly, at low temperatures. An investigation of the role of clustering of these defects and the impact on the predicted thermal conductivity is reserved for future work.

In figure 3 the extrapolated calculated thermal conductivity for both the Li-rich and Li-poor cases are shown. We see the same anisotropy in the thermal conductivity in the three spatial directions, as seen in previous work [26]. The thermal conductivity along z is notably lower than that in x and y. From kinetic theory of a phonon gas in crystal the thermal conductivity can be given as:

$$k = \frac{1}{3} C_v l v \tag{3}$$

where, C_v represents the heat capacity at constant volume, l is the phonon mean free path and v are the phonon velocities. Phonon velocities can be obtained from the Christoffel equation:

$$\left(\Gamma_{ij} - {}^{2}\,\delta_{ij}\right) u_j = 0 \tag{4}$$

and,

$$\Gamma_{ij} = \sum_{k=1}^{3}\sum_{k=1}^{3} C_{ijkl} n_k n_l \tag{5}$$

where, ρ is the density, u_j is the displacement in j, n_k and n_j are the direction cosines and C_{ijkl} is the elastic tensor. Therefore, there is a clear link between the elastic stiffness of the material and the thermal conductivity [44]. Previous work examined the elastic properties of Li_2TiO_3 and showed that the Young's modulus in z (205.7 GPa) is significantly reduced relative to x (238.2 GPa) and y (230.7 GPa) [32]. It should be noted that the orientation of the crystal in this previous work is not the same as used here and so comparisons of the thermal conductivities and stiffness's in x and y are not possible. The reduced stiffness predicted in the z direction will lead to lower phonon velocities reducing the thermal conductivity in this direction. This has the effect of reducing the average thermal conductivity (plotted as a dotted line) downwards.

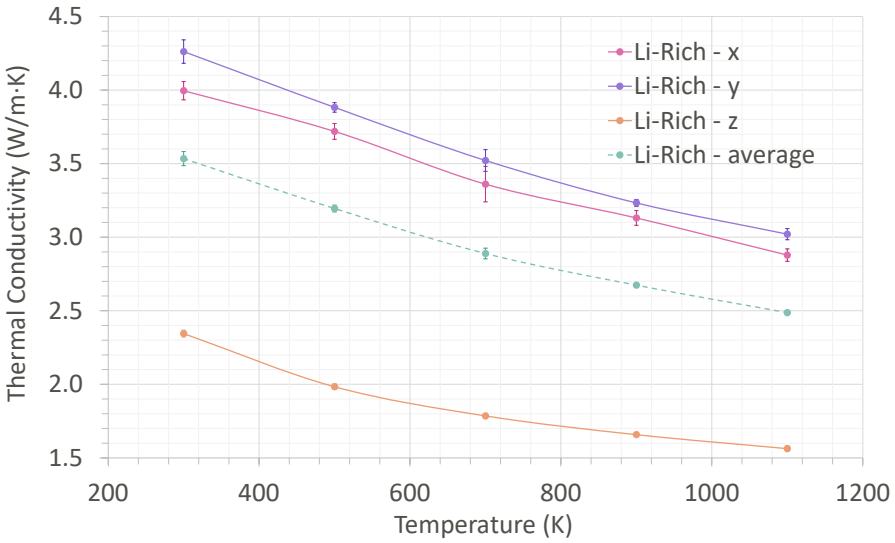

(a) Li-rich

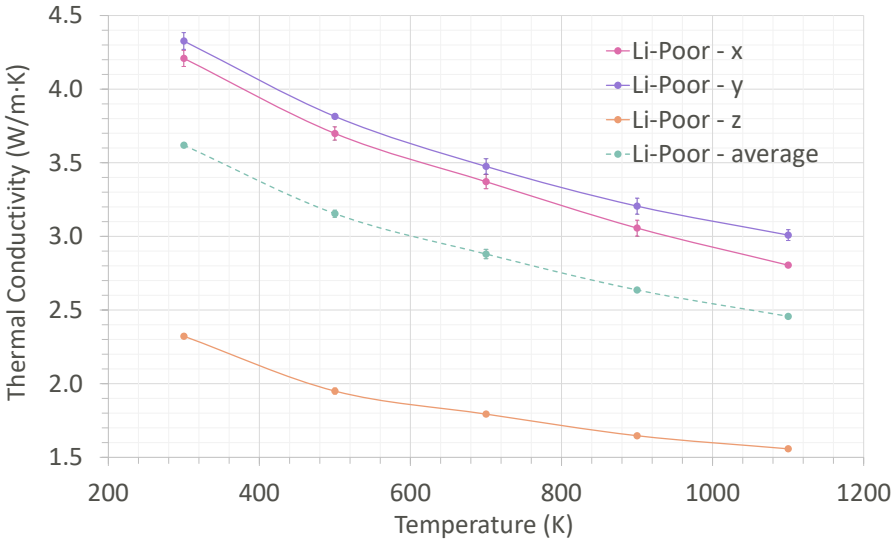

(b) Li-poor

Figure 3: Calculated thermal conductivity of Li-rich and Li-poor as a function of temperature, in each of the spatial directions, and as an average over all directions. Where the Li-rich case has 1% more lithium and the Li-poor case has 1% less lithium than perfect Li_2TiO_3.

Figure 4 shows the average thermal conductivities of the Li-rich and Li-poor

cases are compared to the perfect crystal [26]. From this figure we see that the introduction of defects reduces the thermal conductivity at low temperatures (< 500 K), although this reduction is modest. This is perhaps unsurprising as the antisite defects are not anticipated to have a significant impact on the thermal conductivity [3]. As the temperature increases the thermal conductivity for both non-stoichiometric samples becomes the same as that predicted for the stoichiometric material. Comparing both sides of the stoichiometry, the Li-rich side appears to have a slightly larger effect on the thermal conductivity ($\sim 9\%$ vs $\sim 7\%$ less than the perfect crystal) at 300 K.

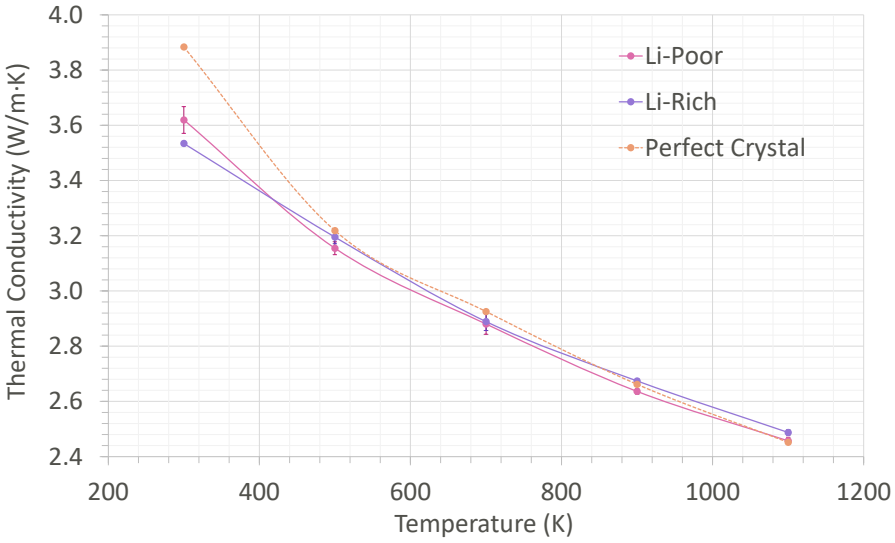

Figure 4: The average calculated thermal conductivity of Li-rich, Li-poor, and perfect Li_2TiO_3 as a function of temperature.

In figure 6, the calculated thermal conductivities of Li-rich, Li-poor and the perfect crystal are displayed for individual x, y, and z-directions. Here we can see how the introduction of defects affected the thermal conductivity in each direction, which is particularly relevant for Li_2TiO_3 due to the high degree of anisotropy predicted previously.

Some experimental data concerning non-stoichiometric Li_2TiO_3 is available

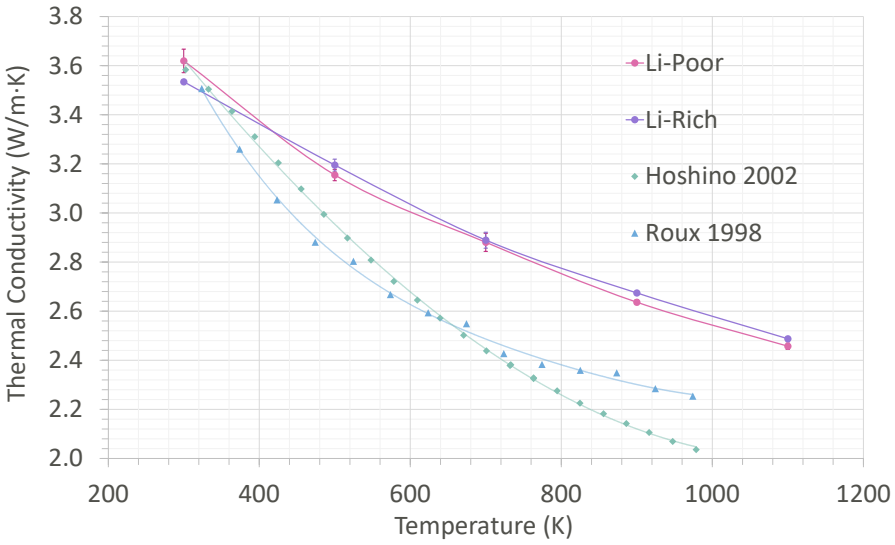

Figure 5: The average calculated thermal conductivity of Li-rich and Li-poor, plotted alongside experimental results from the literature [11, 25].

in the literature. Roux [25] and Hoshino *et al.* [11] measured thermal properties of $0.95Li_2TiO_3$ (where the molecular ratio of Li_2O over TiO_2 is 0.95, i.e. lithium deficient). This is seen compared to this work in figure 5. We see the same trend in the data of decreasing thermal conductivity with increasing temperature. This experimental data is not directly comparable to this work due to the presence of many other defects not included in our simulations. Both Roux and Hoshino *et al.* made the interesting observation of finding the thermal conductivity of lithium deficient Li_2TiO_3 to be higher than the stoichiometric thermal conductivity. As discussed in the introduction the origin of this may be increased grain sizes observed in the non-stoichiometric material, resulting in reduced phonon scattering at grain boundaries [19].

Figure 6 shows that the reduction in thermal conductivity observed at low temperatures is predominantly in the x and y-directions irrespective of whether the sample is Li-rich or Li-poor. By contrast the thermal conductivity in the z-direction shows very little difference between the three cases.

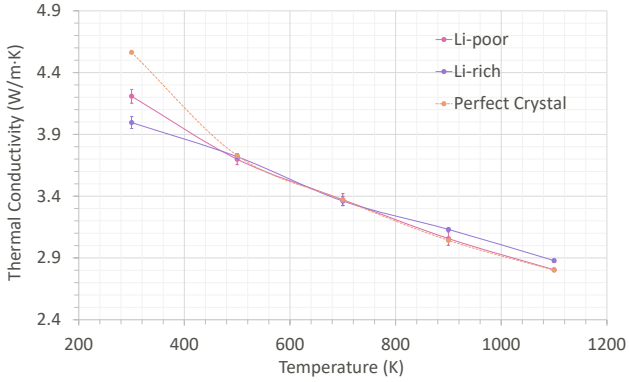

(a) x

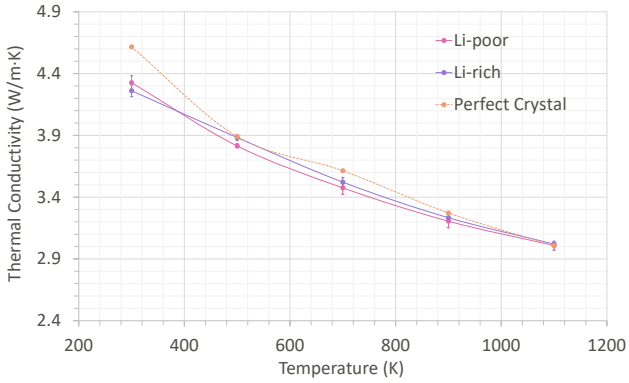

(b) y

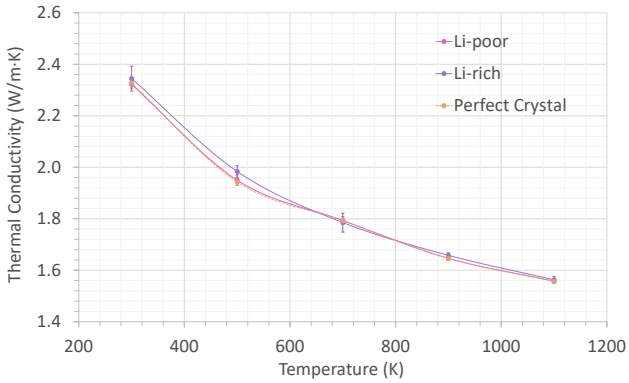

(c) z

Figure 6: Calculated thermal conductivity of Li-rich, Li-poor, and perfect Li_2TiO_3 as a function of temperature, in each of the spatial directions x, y, and z.

4. Conclusion

From defect energies calculated using the Mott-Littleton approach the reaction energies for different mechanisms for incorporation of non-stoichiometry have been determined. The results predict that in the Li_2O-rich regime accommodation is via the mutually charge compensating Li_i^{1+} and Li_{Ti}^{3-} defects, while in the TiO_2 rich regime accommodation is via the V_{Li}^{1-} defect with charge compensation provided by the Ti_{Li}^{3+} defect. The energy for incorporation of a formula unit of Li_2O was found to be significantly lower than for TiO_2, in agreement with the phase diagram that shows considerably more non-stoichiometry on the Li_2O-rich side.

Starting from lowest energy configurations, non-stoichiometry was accommodated in Non-Equilibrium Molecular Dynamics (NEMD) simulations to calculate the thermal conductivity. It was found that the thermal conductivity decreases on both sides of the stoichiometry (1% Li excess and 1% Li loss) at temperatures < 500 K. However, at higher temperatures changes in the stoichiometry of the crystal have a negligible impact on the thermal conductivity. The Li-rich case appears to have a slightly greater effect than the Li-poor case. The previously seen anisotropy of the thermal conductivity of Li_2TiO_3 is seen again, with the non-stoichiometry making no effect to the thermal conductivity in the z-direction, and only affecting the thermal conductivity in x and y. Overall, the results show that the thermal conductivity drops with the introduction of defects accommodating non-stoichiometry for both sides of the stoichiometry.

Given that the breeder blanket region of a future fusion reactor will be operating at higher temperatures, the results presented here suggest that there will be little or no impact from Li burn-up on the thermal conductivity of the breeder material and consequently, no impact on thermal efficiency of the reactor. Further, the changes in stoichiometry were accommodated through the introduction of large numbers of point defects, similar to those introduced by neutron irradiation. As a consequence we speculate that the these defects are also unlikely to significantly impact the thermal conductivity. However,

neutron irradiation can also create much larger defects such as dislocation loops and voids; the impact that those might have on thermal conductivity must be assessed separately in future work.

5. Acknowledgements

This work has been carried out within the framework of the EUROfusion Consortium, funded by the European Union via the Euratom Research and Training Programme (Grant Agreement No 101052200 — EUROfusion). Views and opinions expressed are however those of the author(s) only and do not necessarily reflect those of the European Union or the European Commission. Neither the European Union nor the European Commission can be held responsible for them.

MRG acknowledges funding from the EPSRC Energy Programme [grant number EP/T012250/1]. This work was performed using resources provided by the Cambridge Service for Data Driven Discovery (CSD3) operated by the University of Cambridge Research Computing Service (http://www.csd3.cam.ac.uk), provided by Dell EMC and Intel using Tier-2 funding from the Engineering and Physical Sciences Research Council (capital grant EP/ P020259/1), and DiRAC funding from the Science and Technology Facilities Council (http://www.dirac.ac.uk).

Via our membership of the UK's HEC Materials Chemistry Consortium, which is funded by EPSRC (EP/L000202, EP/R029431), this work used the ARCHER UK National Supercomputing Service (http ://www.archer.ac.uk).

References

[1] R. Knitter, P. Chaudhuri, Y. Feng, T. Hoshino, I.-K. Yu, Recent developments of solid breeder fabrication, Journal of Nuclear Materials 442 (1, Supplement 1) (2013) S420 – S424, fifteenth International Conference on Fusion Reactor Materials.

[2] F. Hernández, P. Pereslavtsev, Q. Kang, P. Norajitra, B. Kiss, G. Nádasi, O. Bitz, A new HCPB breeding blanket for the EU DEMO: Evolution,

rationale and preliminary performances, Fusion Engineering and Design 124 (2017) 882–886, proceedings of the 29th Symposium on Fusion Technology (SOFT-29) Prague, Czech Republic, September 5-9, 2016.

[3] L. Snead, S. Zinkle, D. White, Thermal conductivity degradation of ceramic materials due to low temperature, low dose neutron irradiation, Journal of Nuclear Materials 340 (2) (2005) 187–202.

[4] J.-P. Crocombette, L. Proville, Thermal conductivity degradation induced by point defects in irradiated silicon carbide, Applied Physics Letters 98 (19) (2011) 191905.

[5] M. Qin, S. Middleburgh, M. Cooper, M. Rushton, M. Puide, E. Kuo, R. Grimes, G. Lumpkin, Thermal conductivity variation in uranium dioxide with gadolinia additions, Journal of Nuclear Materials 540 (2020) 152258.

[6] H. Kleykamp, Phase equilibria in the Li–Ti–O system and physical properties of Li_2TiO_3, Fusion Engineering and Design 61-62 (2002) 361–366.

[7] G. Lang, Die kristallstruktur einiger vertreter der verbindungs-klasse $Me^I_2Me^{IV}O_3$ als beitrag zur aufklrung der ordnungsphase von Li_2TiO_3, Zeitschrift für anorganische und allgemeine Chemie 276 (1954) 77–94.

[8] K. Kataoka, Y. Takahashi, N. Kijima, H. Nagai, J. Akimoto, Y. Idemoto, K. Ohshima, Crystal growth and structure refinement of monoclinic Li_2TiO_3, Materials Research Bulletin 44 (1) (2009) 168 – 172.

[9] S. T. Murphy, N. D. M. Hine, Anisotropic charge screening and supercell size convergence of defect formation energies, Physical Review B 87 (2013) 094111.

[10] G. Izquierdo, A. R. West, Phase equilibria in the system Li_2O-TiO_2, Materials Research Bulletin 15 (11) (1980) 1655–1660.

[11] T. Hoshino, M. Dokiya, T. Terai, Y. Takahashi, M. Yamawaki, Nonstoichiometry and its effect on thermal properties of Li_2TiO_3, Fusion Engineering and Design 61-62 (2002) 353–360.

[12] T. Hoshino, K. Kenichi, Y. Natori, F. Oikawa, N. Nakano, M. Nakamura, K. Sasaki, A. Suzuki, T. Terai, K. Tatenuma, Development of advanced tritium breeding material with added lithium for ITER-TBM, Journal of Nuclear Materials 417 (2011) 684–687.

[13] T. Hoshino, Pebble fabrication of super advanced tritium breeders using a solid solution of $Li_{2+x}TiO_{3+y}$ with Li_2ZrO_3, Nuclear Materials and Energy 9 (2016) 221–226.

[14] H. Guo, H. Wang, R. Chen, Y. Gong, M. Yang, D. Ye, Y. Shi, Q. Shi, T. Lu, Characterization of Li-rich Li_2TiO_3 ceramic pebbles prepared by rolling method sintered in air and vacuum, Journal of Nuclear Materials 546 (2021) 152786.

[15] S. Sato, T. Nishitani, C. Konno, Effects of lithium burn-up on TBR in DEMO reactor SlimCS, Fusion Engineering and Design 87 (5) (2012) 680–683, tenth International Symposium on Fusion Nuclear Technology (ISFNT-10).

[16] Y.-z. Hao, Q.-l. Zhang, J. Zhang, C.-r. Xin, H. Yang, Enhanced sintering characteristics and microwave dielectric properties of Li_2TiO_3 due to nano-size and nonstoichiometry effect, J. Mater. Chem. 22 (2012) 23885–23892.

[17] J. Bian, Y. Dong, Sintering behavior, microstructure and microwave dielectric properties of $Li_{2+x}TiO_3$ ($0 \leq x \leq 0.2$), Materials Science and Engineering: B 176 (2) (2011) 147–151.

[18] F. Kröger, H. Vink, Relations between the concentrations of imperfections in crystalline solids, Vol. 3 of Solid State Physics, Academic Press, 1956, pp. 307–435.

[19] K. Mukai, K. Sasaki, T. Hashimoto, A. Suzuki, T. Hoshino, T. Terai, Effect of Li/Ti ratio on microstructure and thermal diffusivity of lithium titanate for solid breeding material, Fusion Engineering and Design 86 (9)

(2011) 2643–2646, proceedings of the 26th Symposium of Fusion Technology (SOFT-26).

[20] S. T. Murphy, N. D. M. Hine, Point defects and non-stoichiometry in Li_2TiO_3, Chemistry of Materials 26 (4) (2014) 1629–1638.

[21] Ģ. Vītiņš, G. Ķizāne, A. Lūsis, J. Tīliks, Electrical conductivity studies in the system Li_2TiO_3-$Li_{1.33}Ti_{1.67}O_4$, Journal of Solid State Electrochemistry 6 (5) (2002) 311–319.

[22] J. Davis, A. Haasz, Thermal diffusivity/conductivity of AECL Li_2TiO_3 ceramic, Journal of Nuclear Materials 232 (1) (1996) 65–68.

[23] S. Saito, K. Tsuchiya, H. Kawamura, T. Terai, S. Tanaka, Density dependence on thermal properties of Li_2TiO_3 pellets, Journal of Nuclear Materials 253 (1) (1998) 213–218.

[24] J. Reimann, S. Hermsmeyer, Thermal conductivity of compressed ceramic breeder pebble beds, Fusion Engineering and Design 61-62 (2002) 345–351.

[25] N. Roux, Proceeding of Sixth International Workshop on Ceramic Breeder Blanket Interactions, 22–24 October 1997, Mito City, Japan (1998) 139.

[26] M. Sanjeev, M. R. Gilbert, S. T. Murphy, Anisotropic thermal conductivity in Li_2TiO_3 ceramic breeder materials, Fusion Engineering and Design 170 (2021) 112710.

[27] M. Born, J. E. Mayer, Zur gittertheorie der ionenkristalle, Zeitschrift für Physik 75 (1932) 1–18.

[28] R. Buckingham, The classical equation of state of gaseous helium, neon and argon, Proceedings of The Royal Society A: Mathematical, Physical and Engineering Sciences 168 (1938) 264–283.

[29] M. Vijayakumar, S. Kerisit, Z. Yang, G. L. Graff, J. Liu, J. A. Sears, S. D. Burton, K. M. Rosso, J. Hu, Combined 6,7 Li NMR and molecular dynam-

ics study of Li diffusion in Li_2TiO_3, The Journal of Physical Chemistry C 113 (46) (2009) 20108–20116.

[30] M. Matsui, M. Akaogi, Molecular dynamics simulation of the structural and physical properties of the four polymorphs of TiO_2, Molecular Simulation 6 (4-6) (1991) 239–244.

[31] B. G. Dick, A. W. Overhauser, Theory of the dielectric constants of alkali halide crystals, Phys. Rev. 112 (1958) 90–103.

[32] S. T. Murphy, P. Zeller, A. Chartier, L. Van Brutzel, Atomistic simulation of the structural, thermodynamic, and elastic properties of Li_2TiO_3, The Journal of Physical Chemistry C 115 (44) (2011) 21874–21881.

[33] N. F. Mott, M. J. Littleton, Conduction in polar crystals. i. electrolytic conduction in solid salts, Trans. Faraday Soc. 34 (1938) 485–499.

[34] J. D. Gale, A. L. Rohl, The general utility lattice program (GULP), Molecular Simulation 29 (5) (2003) 291–341.

[35] S. Plimpton, Fast parallel algorithms for short-range molecular dynamics, J Comp Phys 117 (1995) 1–19.
URL `http://lammps.sandia.gov`

[36] F. Müller-Plathe, A simple nonequilibrium molecular dynamics method for calculating the thermal conductivity, The Journal of Chemical Physics 106 (14) (1997) 6082–6085.

[37] J. Fourier, The analytical theory of heat, Cambridge University Press, 1878.

[38] H. Casimir, Note on the conduction of heat in crystals, Physica 5 (6) (1938) 495 – 500.

[39] C. Oligschleger, J. C. Schön, Simulation of thermal conductivity and heat transport in solids, Phys. Rev. B 59 (1999) 4125–4133.

[40] P. K. Schelling, S. R. Phillpot, P. Keblinski, Comparison of atomic-level simulation methods for computing thermal conductivity, Phys. Rev. B 65 (2002) 144306.

[41] J. Ball, S. Murphy, R. Grimes, D. Bacorisen, R. Smith, B. Uberuaga, K. Sickafus, Defect processes in $MgAl_2O_4$ spinel, Solid State Sciences 10 (6) (2008) 717–724.

[42] C.-L. Yu, D.-P. Gao, K. Yanagisawa, Vacancy and substitution defects of β-Li_2TiO_3 prepared by hydrothermal method, Chemistry Letters 43 (3) (2014) 369–370.

[43] P. Hirel, Atomsk: A tool for manipulating and converting atomic data files, Computer Physics Communications 197 (2015) 212 – 219.

[44] Y. Ding, B. Xiao, Anisotropic elasticity, sound velocity and thermal conductivity of TiO_2 polymorphs from first principles calculations, Computational Materials Science 82 (2014) 202–218.